ADVANCED FUNCTIONAL MATERIALS
www.afm-journal.de

Interfacial Chemistry and Lithiophilicity Design for High Energy Hybrid Li-Ion/Metal Batteries in a Wide Temperature Range

Taiyu Lyu, Meina Huang, Jinping Xu, Xin Lin, Xin Xiao, Lizhe Liang, Cheng Zhang, Dechao Wang, and Zhifeng Zheng**

Hybrid Li-ion/metal batteries can optimize energy density and lifespan. However, hybrid batteries face key obstacles like poor Li reversibility and dendrite growth. Herein, carbon nanofibers encapsulated by graphitized layers decorated with uniformly distributed Ag nanoparticles (G-CF-Ag) are designed, and interfacial chemistry is regulated to enhance the performance of hybrid batteries. The C_{sp2} carbon structure in graphitized layers effectively reduces side reactions with electrolytes, and Ag nanoparticles improve lithiophilicity and induce uniform Li plating/stripping. A weakly solvated electrolyte of 1 M LiFSI-THF-0.5wt.%$LiNO_3$ induces interfacial chemistry to achieve rapid transport of Li-ions under fast charging conditions and low temperatures. Consequently, with a high-capacity Li deposition of 500 mA h g^{-1} (≈1.25 mA h cm^{-2}), the G-CF-Ag||Li delivers an ultra-high plateau capacity of 716 mA h g^{-1} at voltages below 0.1V at 0.2 C, and maintains an average CE of 99.1% over 150 cycles at 2 C fast charging. Notably, the cell continues to operate stably even in a wide temperature range from 50°C to -20°C. Furthermore, at an ultra-low N/P ratio of 0.3, the G-CF-Ag||NCM811 provides a high energy density of 587.5 W h kg^{-1} at 0.2 C. At the same N/P ratio, the G-CF-Ag||LFP maintains stable cycling in a wide temperature range from 50°C to -20°C.

1. Introduction

Traditional Li-ion batteries (LIBs) have played a crucial role in portable electronic devices, electric vehicles, and the field of energy storage.[1,2] Nevertheless, traditional LIBs fall short in meeting the demands of high energy density and operation under extreme conditions (e.g. wide temperature range and fast charging) that are crucial for extending the operating range and cold regions of electric vehicles, portable electronics, and large-scale energy storage systems without significantly increasing the size and weight of the battery packs. The Li metal anode is among the most desirable anodes for high energy density LIBs because it possesses several advantages, including a low density of 0.53 g cm^{-3}, a high theoretical specific capacity of 3860 mA h g^{-1}, and an extremely low standard reduction potential (−3.04 V).[3,4] However, issues such as low Coulombic efficiency (CE) and Li dendrites have severely hampered its development.[5,6]

Carbon material, as a Li metal anode substrate, can be used to fabricate carbon/Li metal composite anode to enhance average CE and inhibit Li dendrite growth.[4,7] However, with a low N/P (Li metal/cathode) ratio, Li metal batteries (LMBs) struggle to maintain a long-term life for hundreds of cycles.[8,9] Hybrid Li-ion/metal batteries (LIB/LMBs) are a new solution that uses less carbon (carbon anode/cathode<1) as the Li-free anode for Li-ion/metal storage mechanism and has a higher energy density than traditional LIBs using carbon anode and LMBs using carbon/Li composite anode (detail in Figure 6a).[10–12] Additionally, hybrid LIB/LMBs reduce cost (less carbon) and avoid harsh environmental requirements for preparing carbon/Li composite anode or Li anode for high energy LMBs.[13,14] However, the Li-ion storage capacity of carbon substrates is restricted, especially in terms of the low-potential capacity within the voltage range of 0–0.1 V. This inevitably leads to a substantial quantity of Li metal participating in the reaction, thereby accelerating its consumption during repeated Li plating/stripping of hybrid LIB/LMBs.[15–17]

In recent years, electrolyte design has been vital for improving the stability and low-potential capacity of hybrid LIB/LMBs. Our

T. Lyu, M. Huang, J. Xu, X. Lin, X. Xiao, C. Zhang, D. Wang, Z. Zheng
Fujian Provincial Industry Technologies Development Base for New Energy
Collaborative Innovation Platform for Energy Storage Technology of Advanced Electrochemical of Fuzhou-Xiamen-Quanzhou National Independent Innovation Demonstration Zone
College of Energy
Xiamen University
Xiamen 361102, P. R. China
E-mail: zhifeng.zheng@xmu.edu.cn

L. Liang
School of Mechanical Engineering
Guangxi University
Nanning 530004, P. R. China
E-mail: lianglizhe@gxu.edu.cn

Z. Zheng
China Fujian Innovation Laboratory of Energy Materials Science and Technology
Tan Kah Kee Innovation Laboratory
Xiamen University
Xiamen 361102, P. R. China

The ORCID identification number(s) for the author(s) of this article can be found under https://doi.org/10.1002/adfm.202500212

DOI: 10.1002/adfm.202500212

group has reported anion-dominated weakly solvated electrolytes that crucially endow carbon anodes with an ultra-high low-potential capacity and a high average CE.[10] The pre-cycled carbon film anodes can exhibit long-term cycling stability over 1000 cycles in hybrid LIB/LMBs full cell. Subsequently, we enhanced the initial Coulombic efficiency (ICE) of the carbon nanofibers film in hybrid LIB/LMBs by designing carbon nanofibers encapsulated by graphitized layers.[18] When fully discharged to 0 V and further plating 300 mA h g^{-1} Li, the hybrid battery demonstrated a high ICE and excellent long-term cycling stability. Up to now, there are reports on designing carbon substrates for hybrid LIB/LMBs, but few have focused on batteries with high Li metal loading (≥500 mA h g^{-1} Li) due to low average CE.[19] Therefore, it is essential to develop high energy hybrid LIB/LMBs with high Li loading (carbon anode/cathode <0.5 and plating Li ≥500 mA h g^{-1}) capable of operating under extreme conditions such as wide temperature range and fast charging. Additionally, it is also important to investigate their energy density and systematically compare it with that of traditional LIBs and LMBs utilizing carbon/Li metal composite anodes. These findings can guide the rational design of hybrid LIB/LMBs or LMBs using carbon substrate to achieve higher energy density.

For these reasons, we collaboratively designed carbon nanofibers encapsulated by graphitized layers decorated with uniformly distributed Ag nanoparticles (G-CF-Ag) through a two-step flash Joule heating (FJH) method and regulated interfacial chemistry to enhance the performance of the hybrid battery. The C_{sp2} carbon structure in graphitized layers effectively reduces side reactions with the electrolyte, and Ag nanoparticles enhance lithiophilicity and induce uniform Li plating/stripping. A weakly solvated electrolyte of 1M LiFSI-THF-0.5 wt.%$LiNO_3$ induces interfacial chemistry to achieve rapid transport of Li-ions. Consequently, under a high-capacity Li deposition of 500 mA h/g (1.25 mA h cm^{-2}), the G-CF-Ag||Li achieves a high ICE of 82.2%, an ultra-high plateau capacity, and excellent rate performance. The G-CF-Ag||Li maintains an average CE of 99.1% over 150 cycles at 2 C fast charging, and operates stably even in a wide temperature range from 50°C to −20°C. Furthermore, at an ultra-low N/P ratio of 0.3, the G-CF-Ag||NCM811 delivers a high discharge capacity of 937.6 mA h g^{-1} and higher energy density of 587.5 W h kg^{-1} compared with LIBs and LMBs models at 0.2 C. At the same N/P ratio, the G-CF-Ag||LFP full cell maintains stable cycling in a wide temperature range from 50°C to −20°C. These lithophilic heterogeneous carbon nanofibers and interfacial chemistry design pave a revolutionary path for Li-free anodes for high energy hybrid LIB/LMBs or for carbon/Li composite anode for LMBs.

2. Results and Discussion

2.1. Fabrication and Characterization

Figure 1a intuitively presents the preparation process of G-CF-Ag. In detail, first, carbon nanofibers (CF) film precursor was prepared using the electrospinning method with lignin phenolic resin.[9] Subsequently, the CF precursor was carbonized in a tube furnace for 2 h to obtain the CF. Second, the CF was subjected to FJH at 1200°C for 5 s. Finally, 0.8 mL of silver acetate solution was uniformly added to the carbon film (after FJH at 1200°C for 5 s) in an infrared dryer, and then FJH at 800 °C for 1 s was performed to fabricate the G-CF-Ag. As a comparison, the carbon nanofibers encapsulated by graphitized layers (G-CF) were obtained by directly heating CF with FJH at 1200 °C for 5 s and 800 °C for 1 s again. Scanning electron microscope (SEM) images show that the CF, G-CF, and G-CF-Ag are self-supporting carbon films composed of overlapping networks of nanofibers (Figure 1b–e; Figure S1, Supporting Information). Such carbon film electrodes are beneficial for electron transport and the infiltration of electrolytes.[18] The internal space of carbon films is conducive to avoiding volume expansion caused during Li deposition.[20,21] The CF and G-CF present a smooth surface (Figure 1b,c; Figure S1, Supporting Information). In contrast, the G-CF-Ag shows nanoparticles uniformly distributed on the surface of nanofibers (Figure 1d,e). Furthermore, transmission electron microscopy (TEM) images further confirm the uniformly distributed nanoparticles on the nanofiber surface corresponding to Ag nanoparticles, and the size of Ag nanoparticles ranges from 3.1 to 12.2 nm (Figure 1f,g; Figure S2, Supporting Information). Besides, the nanofibers are encapsulated by graphitized layers (Figure 1h). In contrast, the CF belongs to a typical amorphous carbon structure (Figure S3, Supporting Information). Energy dispersive X-ray spectroscopy (EDS) images show that the G-CF-Ag contains C, O, and Ag elements, which are uniformly distributed on the surface of nanofibers (Figure 1i,i_1–i_3).

The XRD spectra can reflect the crystal structure of carbon films. In **Figure** 2a, the two broad peaks at ≈24° and 44° indicate that the CF and G-CF are of hard carbon structure.[22] In addition to these two broad peaks, the G-CF-Ag also shows four sharp peaks corresponding to the Ag phase (PDF#00-004-0783). We further employed XPS to analyze the surface compositions of CF, G-CF, and G-CF-Ag. As shown in Figure 2b and Table S1 (Supporting Information), the surface of CF is comprised of 91.2% C atom and 8.8% O atom. In contrast, after FJH treatment, the G-CF exhibits a significantly higher C content of 97.9% and a reduced O content of 2.1%. Similar to G-CF, the G-CF-Ag also exhibits significantly higher C content of 97.0%, O content of 2.0%, and Ag content of 1.0%. The significant differences in the C, O, and Ag components are reflected in the C 1s, O 1s, and Ag 3d spectra. Unlike CF with a low proportion of C_{sp2} and a high proportion of C_{sp3} structure, both G-CF and G-CF-Ag feature a higher proportion of C_{sp2} and a lower proportion of C_{sp3} structure (Figure 2c).[23] The C_{sp2} structure can reduce the decomposition of electrolytes, resulting in higher ICE of the batteries.[18] The O 1s of G-CF and G-CF-Ag exhibit a lower O atomic ratio and no component of COOH compared to that of CF (Figure 2d).[24,25] According to Ag 3d analysis (Figure 2e), it can be concluded that the FJH treatment yields Ag^0 component.[26,27] The C_{sp2} structure and Ag nanoparticles modification of carbon nanofibers can enhance the conductivity of G-CF-Ag (Figure 2f). However, although the C_{sp2} structure can enhance ICE, it makes the G-CF hydrophobic (Figure 2g). Therefore, the introduction of Ag nanoparticles on G-CF can ensure high ICE and greatly improve the hydrophilicity of G-CF-Ag electrode. From N_2 adsorption/desorption isotherms and pore width distribution, the CF has a specific surface area of 12.1 m^2 g^{-1} (Figure 2h). After FJH treatment, the specific surface areas of G-CF and G-CF-Ag are 7.4 and 6.5 m^2 g^{-1}, respectively. Carbon films after FJH treatment can form surface graphitized layers and reduce specific surface

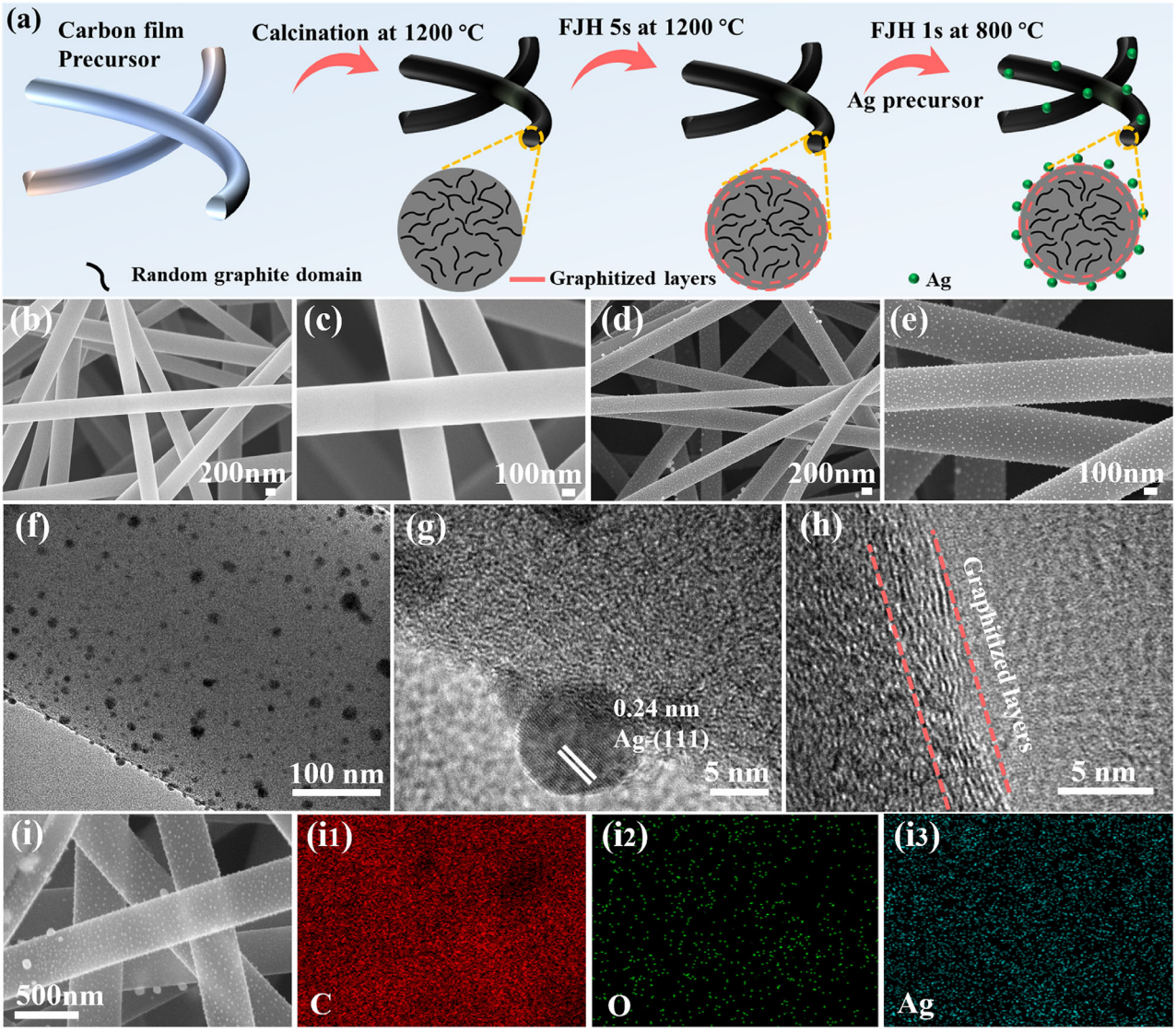

Figure 1. a) Schematic diagram for fabricating the G-CF-Ag. SEM images of the b,c) G-CF and d,e) G-CF-Ag. f) TEM image of the G-CF-Ag. High-resolution TEM images of g) Ag nanoparticle and h) graphitized layers in the G-CF-Ag. i–i_3) EDS images of the G-CF-Ag.

area and pore volume (Figure 2i), effectively reducing the side reactions between carbon films and electrolytes, thereby achieving higher ICE.

Theoretical calculations further emphasize the role of Ag nanoparticles in enhancing the lithophilicity of the G-CF-Ag substrate. As presented in Figure 2j,k, the calculated adsorption energies (E_b) for Li-ions on graphene and Ag (111) are −1.33 and −2.06 eV, respectively. These findings reveal that Ag nanoparticles significantly improve lithophilicity, facilitating the preferential nucleation and growth of Li-ions at nucleophilic sites, which promotes uniform Li plating/stripping behavior.

2.2. Electrochemical Performance

The electrochemical performance of carbon film electrodes, featuring distinct surface characteristics and embedded Ag nanoparticles, was assessed for hybrid Li-ion/metal storage across various electrolytes in a wide temperature range. This evaluation of hybrid Li-ion/metal storage was conducted through a standard full discharge to 0 V, followed by the plating of 500 mA h g^{-1} Li (≈1.25 mA h/cm^2 Li) at a voltage below 0 V. The ICE, rate performance and average CE are key parameters for evaluating hybrid batteries. As shown in **Figure 3**a–c, we first evaluated the ICE of different carbon film electrodes in hybrid storage. In LiFSI-THF-LNO electrolyte, the ICE of CF||Li is 70.8% at 0.2 C (1C = 500 mA h g^{-1}), indicating that the surface defects of hard carbon cause serious side reactions with the electrolyte, resulting in a low ICE (Figure 3a). The encapsulation of graphitized layers endows the G-CF||Li with ICE of 76.4% (Figure S4, Supporting Information). This is mainly due to the high C_{sp2} component of graphitized layers can reduce the reduction of the electrolyte, which is consistent with the results of Cyclic Voltammetry (CV) analysis (Figure S5, Supporting Information).[18]

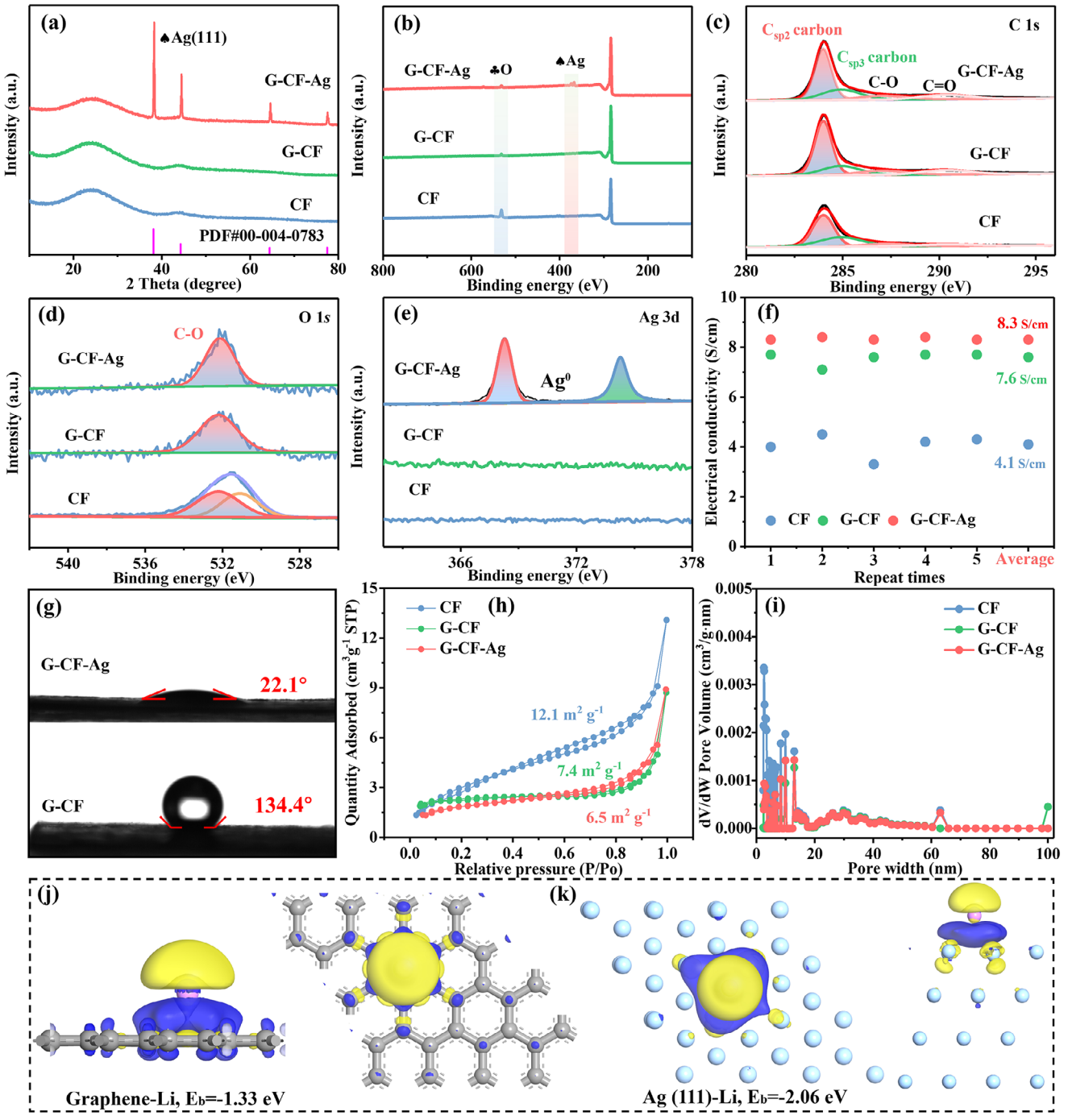

Figure 2. a) XRD spectra. b) XPS, c) C 1s, d) O 1s, and e) Ag 3d of carbon films. f) The electrical resistivities of CF, G-CF, and G-CF-Ag. g) Contact angles between water and carbon films. h) N_2 adsorption/desorption isotherms and corresponding i) pore width distribution of carbon films. Adsorption energy (blue is positive, yellow is negative) and electron charge difference analysis of Li-ion on j) graphene and k) Ag (111).

The G-CF-Ag||Li provides the highest ICE of 82.2% (Figure 3b), mainly due to the synergistic effect of encapsulation of graphitized layers and uniformly distributed Ag nanoparticles. The former reduces the reduction of electrolytes, while the latter improves the reversibility of Li plating/stripping (Figure S5, Supporting Information). In $LiPF_6$-EC-EMC-VC electrolyte, the G-CF-Ag||Li only yields an ICE of 75.4% (Figure 3c). This relatively lower ICE can be attributed to the greater reduction of organic components in ester-based electrolytes during the formation of the solid electrolyte interphase (SEI) layers, compared to the ether-based electrolyte of LiFSI-THF-LNO (detailed discussion in Section 2.3). In addition to the improvement of the ICE, the rate performance results also indicate that the G-CF-Ag||Li (LiFSI-THF-LNO) obtains the highest discharge specific capacity

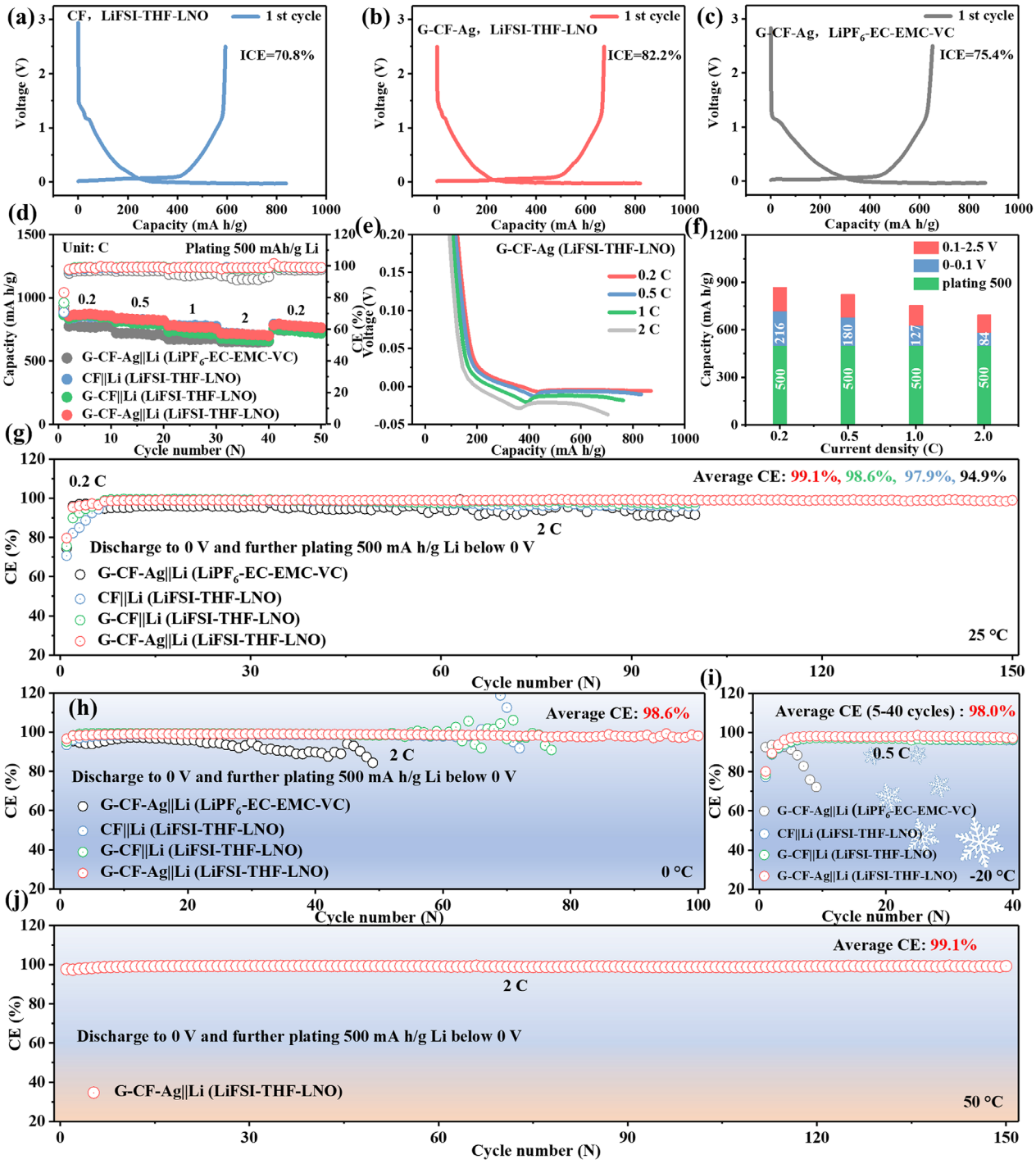

Figure 3. In LiFSI-THF-LNO electrolyte, the 1st charge/discharge curves of a) CF||Li and b) G-CF-Ag||Li at 0.2 C. c) In $LiPF_6$-EC-EMC-VC electrolyte, the 1st charge/discharge curves of G-CF-Ag||Li. d) Rate performance. In LiFSI-THF-LNO electrolyte, e) the 5th cycle discharge curves (−0.05–0.2V) of G-CF-Ag||Li at different current densities, f) corresponding to the slope capacity (2.5–0.1 V), low-potential capacity (0.1–0 V), and plating 500 mA h g^{-1} Li (<0 V). The average CE at g) 2 C at 25°C, h) 2 C at 0°C, i) 0.5 C at −20°C, and j) 2 C at 50°C.

and average CE (within 10 cycles). The G-CF-Ag||Li provides average discharge specific capacities of 863.6, 828.8, 769.8, and 711.0 mA h g^{-1} within 10 cycles at current densities of 0.2, 0.5, 1, and 2 C (Figure 3d), respectively. At the 5th cycle discharge curves of each current density, the G-CF-Ag||Li provides low-potential capacities of 216, 180, 127, and 84 mA h g^{-1} (Figure 3e,f; Figure S6, Supporting Information). That is to say, at voltages less than 0.1V (0–0.1V and plating 500 mA h g^{-1} Li), the G-CF-Ag electrode provides ultra-high capacities of 716, 680, 627, and 584 mA h g^{-1} at current densities of 0.2, 0.5, 1, and 2 C, respectively. This is

unprecedented for carbon-based materials and will greatly increase the energy density of the full cell.

The stability of carbon film electrodes with different surface characteristics in hybrid Li-ion/metal storage was assessed through long-term cycling stability tests at fast charging and in a wide temperature range. As presented in Figure 3g and Figure S7 (Supporting Information), in LiFSI-THF-LNO electrolyte, the G-CF-Ag||Li can achieve an average CE of 99.1% and a high capacity over 700 mA h g^{-1} within 150 cycles at 2 C fast charging at 25°C. In contrast, the CF||Li and G-CF||Li cells only achieve average CEs of 97.9% and 98.6% within 100 cycles at 2 C, respectively. In $LiPF_6$-EC-EMC-VC electrolyte, the G-CF-Ag||Li only offers an average CE of 94.9% within 100 cycles at 2 C at 25°C. In LiFSI-THF-LNO electrolyte, the G-CF-Ag||Li achieves a peak average CE of 98.6% and a high capacity over 650 mA h g^{-1} within 100 cycles at 2 C fast charging at 0°C (Figure 3h; Figure S8, Supporting Information). However, the CF||Li, G-CF||Li, G-CF-Ag||Li ($LiPF_6$-EC-EMC-VC) cells fail after stabilizing for only 60 cycles, 60 cycles, and 30 cycles, respectively. Even under extreme conditions of −20°C, the G-CF-Ag||Li still operates stably and provides the best average CE of 98.0% and a high capacity over 600 mA h g^{-1} compared to the CF||Li and G-CF||Li using LiFSI-THF-LNO electrolyte (Figure 3i; Figure S9, Supporting Information). Conversely, in $LiPF_6$-EC-EMC-VC electrolyte, the G-CF-Ag||Li only cycles 5 times and rapidly fails. Furthermore, at 50°C, the G-CF-Ag||Li (LiFSI-THF-LNO) also provides an average CE of 99.1% and a high capacity over 700 mA h g^{-1} within 150 cycles at 2 C (Figure 3j; Figure S10, Supporting Information). The stability test further confirms that the incorporation of Ag nanoparticles and graphitized layers encapsulated on carbon nanofibers enhances reversibility under the condition of large-amount Li deposition. Additionally, the LiFSI-THF-LNO electrolyte is found to be more compatible with carbon film electrodes in hybrid LIB/LMBs compared to the $LiPF_6$-EC-EMC-VC electrolyte. Under lithiophilicity design and selection of suitable electrolytes, the G-CF-Ag substrate exhibits better long-term cycling performance than reported carbon substrates under extreme conditions (Table S2, Supporting Information).

Observing the morphological changes during or after Li plating/stripping can further reflect the differences in long-term cyclic stability.[28,29] As presented in **Figure 4**, in LiFSI-THF-LNO electrolyte, SEM images present the G-CF-Ag electrode's morphological evolution during hybrid Li-ion/metal storage behavior. The initial G-CF-Ag electrode shows networks of intertwined nanofibers with uniformly distributed Ag nanoparticles (Figure 4a). As the electrode is discharged to 0 V, the nanofiber surface remains smooth despite the formation of SEI layers from the interaction between the nanofiber surface and the electrolyte (Figure 4b). When 500 mA h g^{-1} Li was gradually deposited on the G-CF-Ag electrode below 0 V, Li uniformly nucleated, grew, and coated the nanofiber surface (Figure 4c–e). No dendritic Li was observed. Meanwhile, compared to the initial cross-section, the cross-section of the carbon film also experienced only 102% expansion after depositing 500 mA h g^{-1} Li (Figure S11, Supporting Information), which indicates that the space inside the carbon film can accommodate the deposition of Li metal, thereby reducing volume expansion. During the stripping and charging to 2.5 V, the deposited Li on the nanofibers can be reversibly removed, restoring the smooth nanofiber surface (Figure 4f–h). In situ optical microscopy was also employed to monitor the morphological evolution of Li plating/stripping on the G-CF-Ag electrode at 0.5 mA cm^{-2}. Consistent with the results of SEM images, the microscopic analysis revealed dendrite-free Li throughout all observed stages (Figure 4i–l). Furthermore, after 50 cycles at 2 C, the evolution of electrode morphologies indicates reversibility.[10] The G-CF-Ag electrode presents a small amount of "dead Li" on the nanofibers surface (Figure 4o), whereas the G-CF electrode exhibits a significant increase in "dead Li" (Figure 4n), and the CF electrode has the highest accumulation (Figure 4m) in LiFSI-THF-LNO electrolyte system. This confirms that the G-CF-Ag electrode demonstrates the best reversible Li plating/stripping that is consistent with the stability test results. In the $LiPF_6$-EC-EMC-VC electrolyte system, it was observed that the gaps between the nanofibers of the G-CF-Ag electrode were filled with "dead Li" and Li dendrites (Figure 4p). This further demonstrates that the LiFSI-THF-LNO electrolyte has greater compatibility with carbon film electrodes in hybrid LIB/LMBs than the $LiPF_6$-EC-EMC-VC electrolyte. Figure 4q shows the simplified visualization image of reversible Li-ion/metal storage in the G-CF-Ag electrode using LiFSI-THF-LNO electrolyte. The graphitized layers effectively reduce electrolyte side reactions, and Li-ions can be stored in the nanofibers. As Li deposition starts, Ag nanoparticles induce Li to gradually and uniformly deposit and grow on the nanofiber's surface. Subsequently, the deposited Li can be reversibly stripped.

2.3. Interfacial Chemistry

We can easily understand that introducing uniformly distributed lithiophilic Ag nanoparticles can significantly improve the reversibility of hybrid Li-ion/metal storage.[26] The notable difference in electrochemical performance of the G-CF-Ag between the two electrolytes prompts us to further investigate the interfacial chemistry between the electrolytes and the electrode. The XPS depth sputtering was conducted to reveal the SEI layers composition of G-CF-Ag electrodes after 5 cycles in $LiPF_6$-EC-EMC-VC and LiFSI-THF-LNO electrolytes. In LiFSI-THF-LNO electrolyte, the SEI layers of G-CF-Ag electrode contain C, N, O, S, F, and Li elements in different depth sputtering (**Figure 5**a). In $LiPF_6$-EC-EMC-VC electrolyte, the electrodes' SEI layers contain C, O, F, P, and Li elements in different depth sputtering (Figure 5b). From N 1s spectra, the main components Li_3N and LiN_xO_y are uniformly distributed in the SEI layers of G-CF-Ag electrode in LiFSI-THF-LNO electrolyte (Figure 5c).[10,30,31] The atomic ratios of N are 3.0%, 2.1%, and 1.8% at etching times of 0 s, 35 s, and 70 s, respectively. For F 1s spectra, the electrode's main surface components are LiF and S-F (Figure 5d),[32–34] but with increasing etching time, the main component is LiF in LiFSI-THF-LNO electrolyte. The uniform distribution of Li_3N and LiF enhances the SEI layer's ion conductivity and mechanical properties, effectively minimizing Li dendrite formation and enhancing the reversibility of Li plating/stripping.[10] The $LiPF_6$-EC-EMC-VC, classified as an ester electrolyte, primarily exhibits a solvation structure involving Li, EC, and EMC.[10] The PF_6^- anion has limited participation in this solvation structure, leading to a large reduction of Li-EC/EMC and free PF_6^- during the formation of the SEI layers.[35] Therefore, for F 1s spectra, the

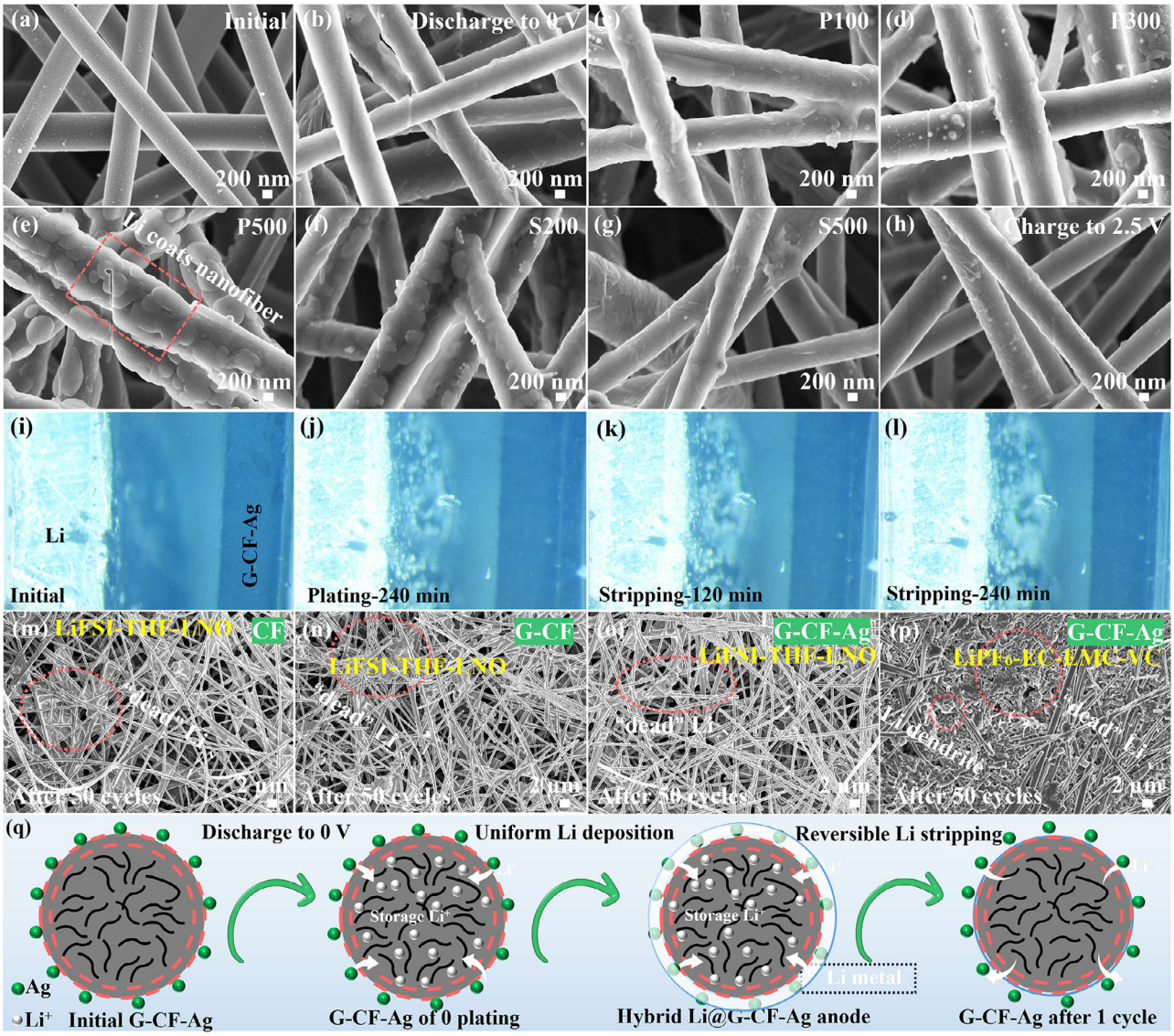

Figure 4. SEM images of the G-CF-Ag electrode at a) the initial state, b) discharged to 0 V, and further plating c) 100 mA h g^{-1} Li, d) 300 mA h g^{-1} Li, and e) 500 mA h g^{-1} Li below 0 V. Then stripping f) 200 mA h g^{-1} Li, g) 500 mA h g^{-1} Li, h) full charge to 2.5 V again in LiFSI-THF-LNO electrolyte. In situ optical microscope images of the morphology evolution of G-CF-Ag electrode after plating Li i) 0 min and j) 240 min, and stripping Li k) 120 min and l) 240 min under 0.5 mA cm^{-2}. SEM images of m) CF, n) G-CF, and o) G-CF-Ag electrodes after 50 cycles in LiFSI-THF-LNO electrolyte. p) SEM image of G-CF-Ag electrode after 50 cycles in $LiPF_6$-EC-EMC-VC electrolyte. q) Schematic diagram of hybrid Li-ion/metal storage behavior of the G-CF-Ag electrode in LiFSI-THF-LNO electrolyte.

electrode's components are LiF, $Li_xPO_yF_z$, and Li_xPF_y (Figure S12a, Supporting Information).[36] For P 2p spectra, the electrode's components are $Li_xPO_yF_z$, Li_xPF_y, P-O (Figure S12b, Supporting Information).[37,38] The presence of $Li_xPO_yF_z$, Li_xPF_y, and more organic components will thicken the SEI layers, reducing the SEI layers' ion conductivity and mechanical strength, thereby impacting electrochemical performance.

High-sensitivity time-of-flight secondary ion mass spectrometry (TOF-SIMS) was further employed to reflect the components and distribution at the interface of G-CF-Ag/electrolytes after 5 cycles. Representative secondary ion fragments (i.e., CH_3O^-, LiF^-, PF_6^-, and $PO_2F_2^-$) were chosen to analyze the decomposition components of the G-CF-Ag electrode/electrolyte interface (Figure 5e,f). The LiF^- represents inorganic LiF obtained through LiFSI or $LiPF_6$ decomposition.[39] The CH_3O^- is used to indicate the presence of solvent decomposition and derived substances.[36] The $PO_2F_2^-$ reflects PF_6^- decomposition.[40] As shown in Figure 5g,h, the 3D-rendering images regarding the differences in component content and distribution of CH_3O^- suggest that the THF solvent exhibits reducible stability in LiFSI-THF-LNO. In contrast, the EC/EMC solvent demonstrates poor reducibility in the $LiPF_6$–EC-EMC-VC, leading to the formation of a greater variety of organic components. This is also reflected in the higher ICE of G-CF-Ag||Li in LiFSI-THF-LNO than in $LiPF_6$-EC-EMC-VC electrolyte. Furthermore, the differences in the content

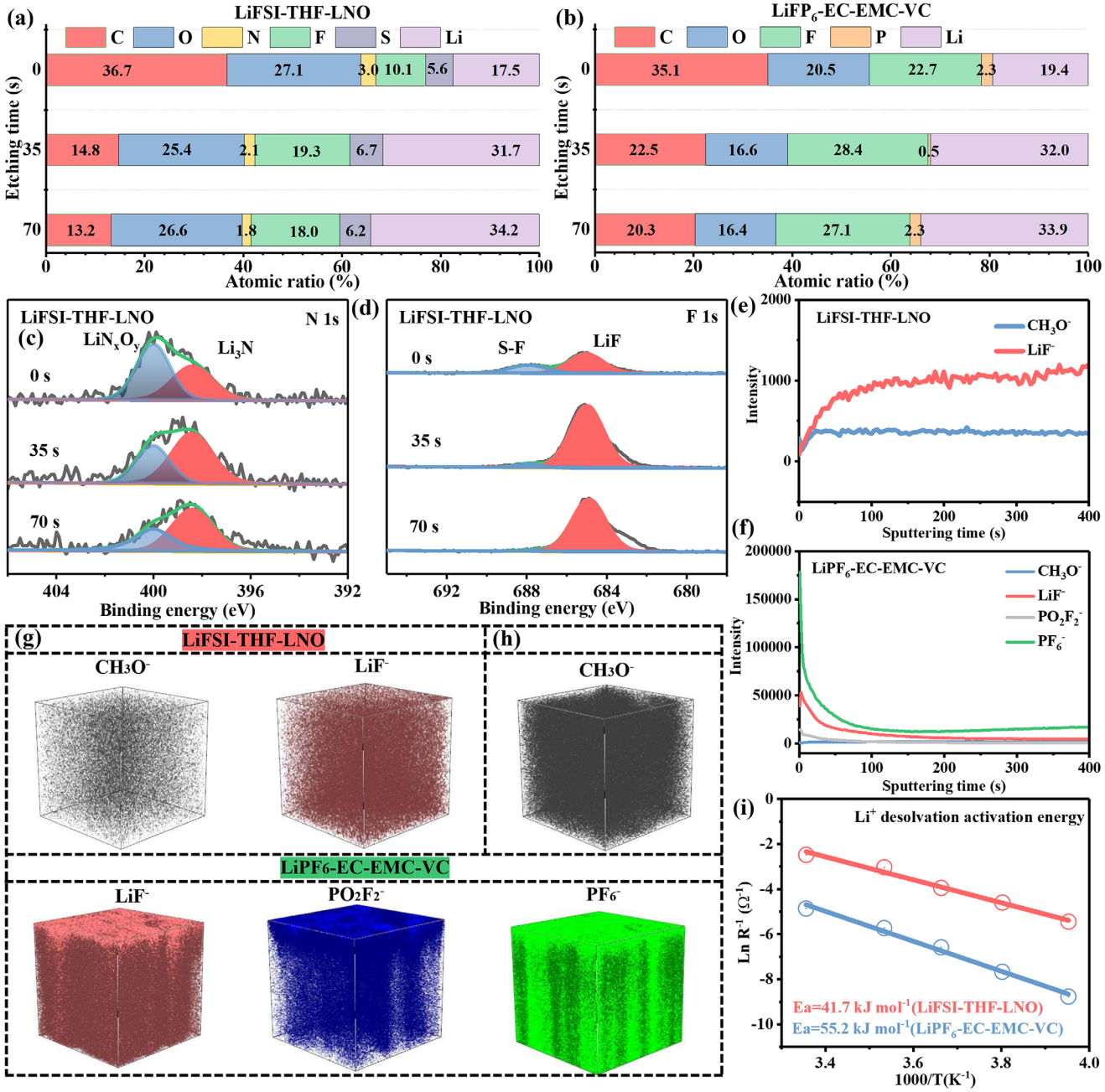

Figure 5. XPS depth sputtering analysis of the composition of the SEI layers formed on the G-CF-Ag electrode in the a) LiFSI-THF-LNO electrolyte and b) $LiPF_6$-EC-EMC-VC electrolyte. High-resolution c) N 1s spectra and d) F 1s spectra of the G-CF-Ag electrode after 5 cycles in LiFSI-THF-LNO electrolyte. The TOF-SIMS measurements of the cycled G-CF-Ag electrode side in the e) LiFSI-THF-LNO and f) $LiPF_6$-EC-EMC-VC electrolytes. Corresponding 3D-rendering images of various fragments. i) Li^+ desolvation activation energy.

and distribution of LiF, PF_6^-, and $PO_2F_2^-$ components indicate that FSI^- participates in the solvation structure, resulting in uniformly distributed LiF components in the LiFSI-THF-LNO. In contrast, in the $LiPF_6$-EC-EMC-VC, PF_6^- remains free and does not participate in solvation, leading to the formation of components like PF_6^- and $PO_2F_2^-$ components, which can compromise the stability and ionic conductivity of the SEI layers. We further performed electrochemical impedance spectroscopy (EIS) on cycled G-CF-Ag||Li using two electrolytes at different temperatures to investigate the impact of the resulting interfacial layers on Li-ion transport. The EIS value of G-CF-Ag||Li in LiFSI-THF-LNO electrolyte is much lower than that in $LiPF_6$-EC-EMC-VC electrolyte, especially under low-temperature conditions (Figure S13, Supporting Information). The calculated desolvation energies of G-CF-Ag||Li using LiFSI-THF-LNO and $LiPF_6$-EC-EMC-VC are 41.7 and 55.2 kJ mol^{-1} (Figure 5i), respectively. Moreover, from galvanostatic intermittent titration technique (GITT) data (Figure S14, Supporting Information),

the Li^+ diffusion coefficient in the G-CF-Ag||Li (LiFSI-THF-LNO) is higher than in the G-CF-Ag||Li ($LiPF_6$-EC-EMC-VC), further verifying the rapid Li storage kinetics achieved in the LiFSI-THF-LNO electrolyte. These indicate a lower energy barrier for Li^+ desolvation in the LiFSI-THF-LNO electrolyte, promoting the rapid transport of Li^+ and Li^+-THF co-intercalates into the G-CF-Ag electrode to achieve ultra-high low-potential capacity than that of the G-CF-Ag||Li using $LiPF_6$-EC-EMC-VC electrolyte during fast charging and at extremely low temperatures.[10,41] Therefore, under larger Li loads (500 mA h g^{-1} Li, ≈1.25 mA h cm^{-2}), a collaborative strategy, which involves the weakly solvated electrolyte of LiFSI-THF-LNO inducing interfacial chemistry and the lithiophilic design of Ag nanoparticles, can effectively improve the performance of hybrid LIB/LMBs.

2.4. The Impact of Li-Ion Storage Mechanism on the Energy Density of Full Cell

As shown in **Figure 6**a, carbon-based anodes have three types of Li storage mechanisms. The first is the traditional LIBs with an N/P ratio greater than 1. The second is the hybrid LIB/LMBs with an N/P ratio less than 1. The third, with an N/P ratio less than 1 and a small amount of Li loaded on the carbon substrate (the overall mass of the carbon/Li composite anode needs to be similar to or less than that of the traditional LIBs carbon anode to achieve higher energy density), are the LMBs. These differences lead to different full cell energy densities. However, there was no in-depth analysis previously. Thus, we used the G-CF-Ag substrate to explore to design anodes and to develop higher energy-density batteries. As shown in Figure 6b, in the Li-ion storage model (N/P = 1.1), the G-CF-Ag||NCM811 full cell provides an ICE of 80.8% and a relatively low energy density of 452.2 W h/kg (based on the active mass of anode and cathode, the energy densities mentioned later are all calculated based on this) at 0.2 C. In the hybrid LIB/LMBs model, the lower the N/P ratio, the higher the energy density. We designed an N/P ratio of 0.3 to obtain a relatively ideal energy density. The G-CF-Ag||NCM811 full cell shows two distinct curve parts: Li-ion storage behavior and Li metal behavior (Figure 6c). The voltage plateau of the former is relatively low. This cell provides an ICE of 80.5% and a discharge capacity of 937.6 mA h g^{-1} with an energy density of 587.5 W h kg^{-1} at 0.2 C. The energy density of hybrid LIB/LMBs is 130% of traditional LIBs. It can be found that the design of the carbon substrate will greatly affect the ICE and charge-discharge curves of hybrid LIB/LMBs. Therefore, developing carbon substrates with high ICE and a high low-potential platform capacity is the key for hybrid LIB/LMBs to maintain high energy density. Meanwhile, we also designed hybrid batteries with different N/P ratios to compare with traditional LIBs (Figure 6e and Figure S15, Supporting Information). When N/P is 0.5, the energy density of the hybrid battery is 124% of that of LIBs (Figure S15b, Supporting Information). When N/P is 0.8, the energy density of the hybrid battery is 112% of that of LIBs (Figure S15a, Supporting Information). In LMBs model, we designed the G-CF-Ag@Li composite anode with a carbon/cathode ratio of 0.3 and a Li metal/cathode ratio of 1 to achieve a higher energy density than traditional LIBs. As shown in Figure 6d, the charge-discharge curve of the G-CF-Ag@Li||NCM811 full cell completely exhibits Li metal behavior. The cell achieves an ICE of 81.0% and the energy density is 563.5 W h kg^{-1} at 0.2 C. By comparing hybrid LIB/LMBs, LIBs, and LMBs, the LIB/LMBs still provide the highest energy density at an N/P ratio of 0.3. Furthermore, the hybrid LIB/LMBs can avoid the harsh environmental requirements for preparing carbon/Li composite anodes. The manufacturing steps of hybrid LIB/LMBs are consistent with those of traditional LIBs with carbon anode. In order to fully exert the high energy density of hybrid LIB/LMBs, the carbon-based anodes should meet the characteristics of high ICE, high low-potential capacity, and excellent stability. In addition, other LMBs strategies such as solid-state electrolytes and liquid electrolytes can be combined to achieve higher energy density and safety in hybrid LIB/LMBs.

Long cycle stability is also used to reflect the performance of hybrid LIB/LMBs. We matched the pre-activated G-CF-Ag with LFP cathode to form full cells. Figure 6f shows that the G-CF-Ag||LFP (LiFSI-THF-LNO) achieves an ICE of 86.5%, a discharge capacity of 752.8 mAh g^{-1}, and a high voltage platform, remaining stable over 50 cycles at 1 C (Figures S16 and S17, Supporting Information). The EIS value of the G-CF-Ag||LFP full cell also demonstrates a gradual decrease with increasing cycle counts (Figure S18, Supporting Information), indicating good interfacial stability. By comparison, the CF||LFP (LiFSI-THF-LNO) exhibits a lower capacity after the same number of cycles. The G-CF-Ag||LFP ($LiPF_6$-EC-EMC-VC) shows a lower capacity and rapid decay after just 10 cycles at 1 C. Even under extreme conditions of −20°C, the G-CF-Ag||LFP (LiFSI-THF-LNO) still operates stably and provides a discharge capacity of 452.8 mAh g^{-1} and a high voltage platform at 0.5 C (Figure 6g,h; Figure S19, Supporting Information). In addition, the G-CF-Ag||LFP full cell can also operate stably even at 1 C at 50°C (Figure S20, Supporting Information). At the same time, the G-CF-Ag substrate is also a promising Li metal substrate. When the N/P ratio is 3, the G-CF-Ag@Li||LFP can stably cycle more than 100 times (Figure S21, Supporting Information). It has been demonstrated that the interfacial chemistry and the lithiophilic Ag nanoparticles design can effectively enhance the ICE, stability, and energy density of hybrid LIB/LMBs at an ultra-low N/P of 0.3.

3. Conclusion

In conclusion, we adopt a collaborative strategy that involves designing uniformly distributed Ag nanoparticles on carbon nanofibers encapsulated by graphitized layers and favorable interfacial chemistry to enhance the performance of hybrid LIB/LMBs under high loading of Li metal. The C_{sp2} carbon structure in graphitized layers effectively reduces side reactions with the electrolyte, and Ag nanoparticles improve lithiophilicity and induce uniform Li plating/stripping. A weakly solvated electrolyte of 1M LiFSI-THF-0.5 wt.%$LiNO_3$ induces interfacial chemistry to achieve rapid transport of Li-ions during fast charging and at low temperatures. As a result, under 500 mA h g^{-1} (≈1.25 mA h cm^{-2}) high-capacity Li deposition, the G-CF-Ag||Li delivers an ultra-high plateau capacity at a voltage of 0-0.1V, offers an average CE of 99.1% over 150 cycles at 2 C fast charging, and operates stably in a wide temperature range from 50°C to −20°C. Furthermore, at an ultra-low N/P ratio of 0.3, the G-CF-Ag||NCM811 provides a higher energy density of 587.5 W h kg^{-1} than that of LIBs and LMBs at 0.2 C. The G-CF-Ag||LFP

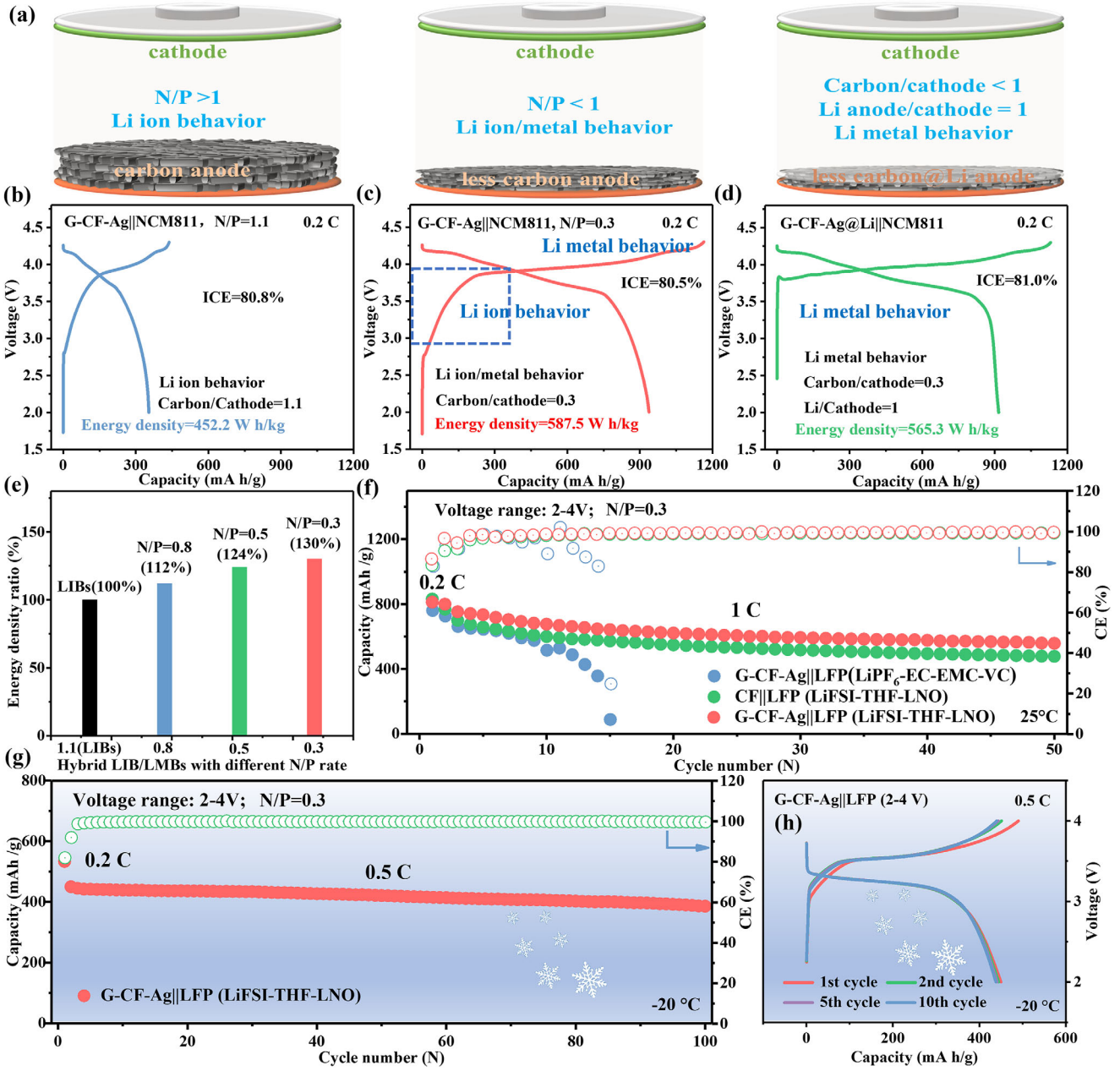

Figure 6. a) Schematic diagrams of carbon anodes for traditional LIBs, hybrid LIB/LMBs, and LMBs under the same cathode loading. The energy densities of b) G-CF-Ag||NCM811(LIBs, N/P = 1.1), c) G-CF-Ag||NCM811(LIB/LMBs, N/P = 0.3, free-Li anode), and d) G-CF-Ag@Li||NCM811(LMBs, carbon/cathode = 0.3, Li metal/cathode = 1) at 0.2 C. e) A comparison of the energy densities between hybrid LIB/LMBs with different N/P ratios and traditional LIBs. f) The long-term cycling stability of different full cells at 1 C at 25°C. g) In LiFSI-THF-LNO electrolyte, the long-term cycling stability of G-CF-Ag||LFP at 0.5 C at −20°C, and h) corresponding charge/discharge curves.

full cell can operate stably in a wide temperature range from 50°C to −20°C. This work provides a significant reference for the design of advanced Li-free carbon anodes for high energy density hybrid LIB/LMBs by interfacial chemistry and lithiophilicity design.

Supporting Information

Supporting Information is available from the Wiley Online Library or from the author.

Acknowledgements

The work was supported by the Science and Technology plan of Fujian Provincial, China (2022G02020 and 2022H6002), the Collaborative Innovation Platform Project for Advanced Electrochemical Energy Storage Technology, the Fuxiaquan National Independent Innovation Demonstration Zone (3502ZCQXT2022001), the Significant Science and Technology Project of Xiamen (the Future Industrial Area) (3502Z20231058) and the Scientific Research Startup Funding for Special Professor of Minjiang Scholars.

Conflict of Interest

The authors declare no conflict of interest.

Data Availability Statement

The data that support the findings of this study are available from the corresponding author upon reasonable request.

Keywords

Ag nanoparticle, graphitized layers encapsulated carbon nanofiber, hybrid Li-ion/metal battery, interfacial chemistry, wide temperature range

Received: January 3, 2025
Revised: February 25, 2025
Published online:

[1] Z. Yang, J. Zhang, M. C. W. Kintner-Meyer, X. Lu, D. Choi, J. P. Lemmon, J. Liu, *Chem. Rev.* **2011**, *111*, 3577.
[2] H. Kwon, J.-H. Lee, Y. Roh, J. Baek, D. J. Shin, J. K. Yoon, H. J. Ha, J. Y. Kim, H.-T. Kim, *Nat. Commun.* **2021**, *12*, 5537.
[3] J.-G. Zhang, W. Xu, J. Xiao, X. Cao, J. Liu, *Chem. Rev.* **2020**, *120*, 13312.
[4] T. Lyu, F. Luo, D. Wang, L. Bu, L. Tao, Z. Zheng, *Adv. Energy Mater.* **2022**, *12*, 2201493.
[5] H. Chen, Y. Yang, D. T. Boyle, Y. K. Jeong, R. Xu, L. S. de Vasconcelos, Z. Huang, H. Wang, H. Wang, W. Huang, H. Li, J. Wang, H. Gu, R. Matsumoto, K. Motohashi, Y. Nakayama, K. Zhao, Y. Cui, *Nat. Energy* **2021**, *6*, 790.
[6] S. Jin, Y. D. Ye, Y. J. Niu, Y. S. Xu, H. C. Jin, J. X. Wang, Z. W. Sun, A. M. Cao, X. J. Wu, Y. Luo, H. X. Ji, L. J. Wan, *J. Am. Chem. Soc.* **2020**, *142*, 8818.
[7] Y. Liu, C. Sun, Y. Lu, X. Lin, M. Chen, Y. Xie, C. Lai, W. Yan, *Chem. Eng. J.* **2023**, *451*, 138570.
[8] T. Lyu, F. Luo, Z. Wang, F. Jiang, S. Geng, Y. Zhuang, X. Lin, J. Chen, D. Wang, L. Bu, L. Tao, L. Liang, Z. Zheng, *Chem. Eng. J.* **2023**, *466*, 143357.
[9] L. Tao, A. Hu, Z. Yang, Z. Xu, C. E. Wall, A. R. Esker, Z. Zheng, F. Lin, *Adv. Funct. Mater.* **2020**, *30*, 2000585.
[10] T. Lyu, F. Luo, L. Liang, D. Wang, L. Tao, Z. Zheng, *Adv. Energy Mater.* **2024**,*14*, 2304520.
[11] C. Martin, M. Genovese, A. J. Louli, R. Weber, J. R. Dahn, *Joule* **2020**, *4*, 1296.
[12] G. Park, S. Kim, J. Kim, S. Bae, Y. Heo, D. Park, H. Kim, J. Shin, J. Moon, J. W. Choi, *Adv. Energy Mater.* **2024**, *14*, 2401289.
[13] K. Hatzell, W. Chang, W. Bao, M. Cai, T. Glossmann, S. Kalnaus, B. Liaw, Y. S. Meng, R. Mohtadi, Y. Wang, *Joule* **2024**, *8*, 1550.
[14] J. Peng, J. Wang, X. Pu, J. Xie, *J. Mater. Chem. A* **2025**, *13*, 928.
[15] H. Gong, Y. Chen, S. Chen, C. Xu, Y. Yang, Y. Ye, Z. Huang, R. Ning, Y. Cui, Z. Bao, *ACS Energy Lett.* **2022**, *7*, 4417.
[16] T. Li, Y. Cao, Q. Song, L. Peng, X. Qin, W. Lv, F. Kang, *Small* **2024**, *20*, 2403057.
[17] B. Seo, D. Kim, S. Park, D. Shin, K. Kim, W. Choi, *Energy Storage Mater.* **2025**, *74*, 103961.
[18] T. Lyu, L. Liang, K. Liu, F. Luo, Q. Fan, P. Guo, D. Wang, G. Wei, L. Tao, Z. Zheng, *Small* **2025**, *21*, 2412457.
[19] X. Yue, J. Zhang, Y. Dong, Y. Chen, Z. Shi, X. Xu, X. Li, Z. Liang, *Angew. Chem., Int. Ed.* **2023**, *62*, 202302285.
[20] J. Zhang, H. Chen, M. Wen, K. Shen, Q. Chen, G. Hou, Y. Tang, *Adv. Funct. Mater.* **2022**, *32*, 2110110.
[21] W. Go, M.-H. Kim, J. Park, C. H. Lim, S. H. Joo, Y. Kim, H.-W. Lee, *Nano Lett.* **2019**, *19*, 1504.
[22] T. Lyu, L. Liang, P. K. Shen, *J. Colloid Interface Sci.* **2021**, *604*, 168.
[23] J. Kang, Y. Ko, J. P. Kim, J. Y. Kim, J. Kim, O. Kwon, K. C. Kim, D. W. Kim, *Nat. Commun.* **2023**, *14*, 901.
[24] L. Tao, Z. Xu, C. Kuai, X. Zheng, C. E. Wall, C. Jiang, A. R. Esker, Z. Zheng, F. Lin, *Energy Storage Mater.* **2020**, *24*, 129.
[25] C. Guo, Z.-H. Luo, M.-X. Zhou, X. Wu, Y. Shi, Q. An, J.-J. Shao, G. Zhou, *Small* **2023**, *19*, 2301428.
[26] Y. J. Fang, S. L. Zhang, Z. P. Wu, D. Y. Luan, X. W. Lou, *Sci. Adv.* **2021**, *7*, eabg3626.
[27] Y. R. Shi, X. F. Hu, Z. Zhang, Y. W. Sun, S. B. Xu, B. Zhao, Y. Xu, Y. L. He, J. J. Zhang, Y. Jiang, *Chem. Eng. J.* **2024**, *500*, 157202.
[28] T. Xie, B. Liang, L. Wu, H. Chen, W. Ye, J. Chen, J. He, H. Xiao, K. Yan, Z. Tan, J. Yang, Y. Li, S. Xiong, S. Huang, *Nano Energy* **2024**, *129*, 110081.
[29] Y. Zhou, X. Zhang, Y. Ding, L. Zhang, G. Yu, *Adv. Mater.* **2020**, *32*, 2005763.
[30] Y. Ouyang, S. Huang, N. Li, S. Lu, Y. Lv, Y. Liu, F. Kang, Y. Cao, *Carbon* **2024**, *229*, 119452.
[31] K. Ding, E. J. Begin, S. Yuan, M. Zhong, Y. Wang, Y. Zhang, X. Zeng, J. L. Bao, Y. Wang, *Adv. Energy Mater.* **2023**, *13*, 2302443.
[32] H. Shen, T. Yu, P. Tang, H. Yang, J. Tan, S. Bai, F. Li, *Adv. Mater.* **2024**, *36*, 2306553.
[33] A.-M. Li, O. Borodin, T. P. Pollard, W. Zhang, N. Zhang, S. Tan, F. Chen, C. Jayawardana, B. L. Lucht, E. Hu, X.-Q. Yang, C. Wang, *Nat. Chem.* **2024**, *16*, 922.
[34] J. Chen, Y. Shen, C. Meng, H. Chen, S. Huang, A. Yuan, J. Qiu, H. Zhu, H. Zhou, *J. Colloid Interface Sci.* **2024**, *653*, 189.
[35] H. Cheng, Q. Sun, L. Li, Y. Zou, Y. Wang, T. Cai, F. Zhao, G. Liu, Z. Ma, W. Wahyudi, Q. Li, J. Ming, *ACS Energy Lett.* **2022**, *7*, 490.
[36] Y. Chen, Z. Ma, Y. Wang, P. Kumar, F. Zhao, T. Cai, Z. Cao, L. Cavallo, H. Cheng, Q. Li, J. Ming, *Energy Environ. Sci.* **2024**, *17*, 5613.
[37] C. Wang, Y. Xie, Y. Huang, S. Zhou, H. Xie, H. Jin, H. Ji, *Angew. Chem., Int. Ed.* **2024**, *63*, 20240230.
[38] A. Huang, Z. Ma, P. Kumar, H. Liang, T. Cai, F. Zhao, Z. Cao, L. Cavallo, Q. Li, J. Ming, *Nano Lett.* **2024**, *24*, 7499.
[39] L. Dong, S. Zhong, B. Yuan, Y. Li, J. Liu, Y. Ji, D. Chen, Y. Liu, C. Yang, J. Han, W. He, *Angew. Chem., Int. Ed.* **2023**, *62*, 202301073.
[40] R. Sim, L. Su, A. Dolocan, A. Manthiram, *Adv. Mater.* **2024**, *36*, 2311573.
[41] Y. Yang, Z. Yang, Z. Li, J. Wang, X. He, H. Zhao, *Adv. Energy Mater.* **2023**, *13*, 2302068.